

# Absorption performance optimization of perforated plate using multiple-sized holes and a porous separating partition



Ki Hyun Kim, Gil Ho Yoon\*

School of Mechanical Engineering, Hanyang University, 222 Wangsimni-ro, Seongdong-gu, 04763 Seoul, Republic of Korea

## ARTICLE INFO

### Article history:

Received 6 July 2016

Received in revised form 11 October 2016

Accepted 5 January 2017

Available online 17 January 2017

### Keywords:

Perforated plate

Multiple-sized holes

Porous separating partition

Wide-band absorption performance

Optimization

Finite element analysis

## ABSTRACT

This research proposes a new type of sound absorptive perforated plate with multiple-sized holes and a porous separating partition in an attempt to extend the sound absorption bandwidth. Separating different sized holes with a porous partition instead of a conventional rigid partition is an unprecedented idea. However, existence of a porous separating partition makes it hard to use theoretical surface impedance models to predict absorption performance. So we introduce appropriate finite element simulation method using the effective density of hole. To consider the end correction effects for hole length and viscosity length of a perforated plate, the effective density of the Johnson-Champoux-Allard model is modified and the end correction lengths of the modified effective density are corrected again in connection with finite element simulation. Material property of a porous separating partition is modeled by the Delany-Bazley material model. After constructing the finite element model, we analyzed the absorption coefficient graphs of perforated plates with two-sized holes and four-sized holes according to the separating partition types: no partition, rigid partition and porous partition. To enhance the wide-band absorption performance, flow resistivity value and thickness of a porous separating partition as well as hole sizes are optimized. From the analysis and design examples, we confirmed that the perforated plate using multiple-sized holes and a porous separating partition can make a continuous frequency range of high absorption coefficient compared to the perforated plate with a conventional rigid partition.

© 2017 Elsevier Ltd. All rights reserved.

## 1. Introduction

This research presents a new type of perforated plate consisting of various-sized holes and a porous separating partition to extend the frequency region of high sound absorption coefficient. In several relevant researches, a variety of novel ideas, such as multi-layer perforated plates, different cavity depths with separating partitions, and internal porous layers, have been investigated based on theoretical and experimental approaches in attempts to improve the wide-band absorption performance [1–9]. Other types of perforated plate systems have also been devised and investigated [10–20]. One of the advantages of the present perforated plate system compared to the previous absorbers is that it shows higher absorption coefficients for a wide frequency range without using a large number of different sized holes. This aspect is vital in case of some area or space limitations. Also it does not increase the required space between the perforated plate and the rigid wall.

### 1.1. Previous perforated plate models for wide-band absorption performance

An important research topic related to the performance of perforated plates is to investigate the method to widen the frequency range of high absorption coefficient. To achieve this, various types of perforated plates have been proposed, as shown in Fig. 1. In [1–5], multi-layers of perforated plates with different-sized holes were proposed (Fig. 1a). For the theoretical prediction of the absorption performance of multi-layer absorbers, some analytical models were proposed and compared with experimental results. Using case studies, researchers have shown significantly improved absorption effects in a wide-band frequency region with some peak frequencies. Other researchers have utilized parallel arrangement of perforated plate modules with different cavity depths that are separated by a rigid partition, as shown in Fig. 1b [6–9]. The idea of different cavity depths can be simply explained by the fact that it utilizes multiple Helmholtz resonance frequencies to widen the high absorption frequency region. However, the designs in Fig. 1a and b are novel with sufficient spaces behind the perforated plates to widen the frequency range over which the plates are most effective. With spatial limitation in the cavity depth behind the

\* Corresponding author.

E-mail addresses: [ghy@hanyang.ac.kr](mailto:ghy@hanyang.ac.kr), [gilho.yoon@gmail.com](mailto:gilho.yoon@gmail.com) (G.H. Yoon).

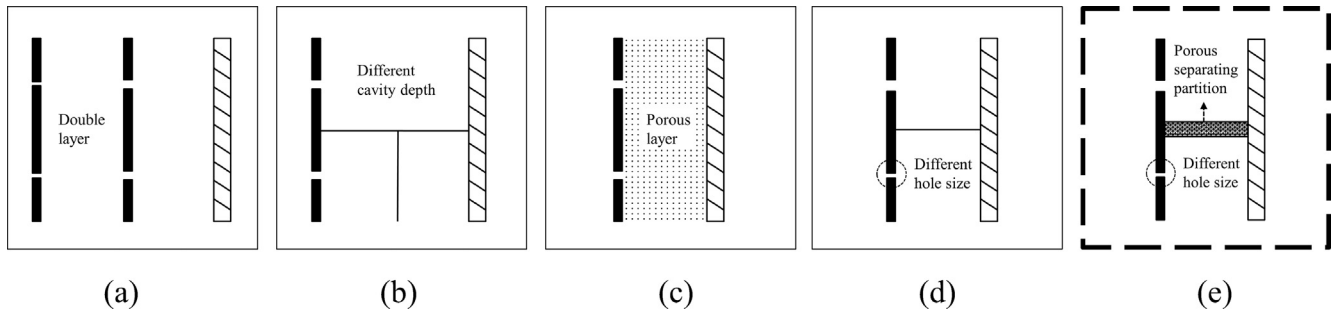


**Fig. 1.** Existing perforated plate models and our suggested perforated plate model. (a) Perforated plate with multi-layers [1–5], (b) perforated plate with different cavity depths separated by a rigid partition [6–9], (c) perforated plate with an internal porous layer [1,10–13], (d) perforated plate with multiple hole sizes separated by a rigid partition (resonator array panel) [14,15], and (e) the suggested perforated plate with multiple hole sizes separated by a porous partition.

plates, it is challenging to realize effective absorption performance in a wide frequency range.

To improve the absorptivity without increasing the space behind the perforated plate, an internal porous layer can be inserted behind the perforated plate, as shown in Fig. 1c [1,10–13]. This is one of the simplest methods that can be used to enhance the sound absorptivity without increasing the thickness of the entire perforated plate structure. However, from an engineering point of view, this method only increases the amplitude of absorption coefficient; it does not adjust the effective frequency range of high absorptivity.

As a different way to avoid the increased entire thickness of a perforated plate structure, a perforated plate with a rigid separator between different-sized holes was proposed in Fig. 1d [14,15]. In [15], a perforated plate with multiple-sized holes, but without a partition, was also proposed. And it was discussed that a perforated plate with multiple-sized holes without a partition performs similarly to a perforated plate with single-sized holes; this is also re-investigated in the present study. In those papers, a specific explanation about the properties of the separating partition was not mentioned. However, by guessing the context, it can be known that the partition is rigid (it is not a porous partition surely). Because one perforated plate module (with single-sized holes) is a single resonator, the parallel arrangement of each module with different-sized holes separated by rigid partitions is a combination of multiple Helmholtz resonators with different resonance frequencies. Therefore, this perforated plate model shows wide-band frequency noise attenuation characteristics of a resonator array panel. Nevertheless, if there is insufficient area to utilize a large number of resonators with different resonance frequencies, it is difficult to obtain wide-band frequency absorption characteristics because each resonator is effective near its resonance frequency.

### 1.2. New perforated plate model with multiple-sized holes and a porous separating partition

To contribute to the wide-band absorption issue of a perforated plate, we propose to use a porous separating partition rather than a rigid separating partition, as shown in Fig. 1e; specifically, we suggest a perforated plate with multiple-sized holes and a porous separating partition. To our knowledge, no previous research has been conducted that predicts the noise attenuation performance of a porous separating partition behind a perforated plate. Using a porous separating partition can lead to effects that are similar to those obtained by using many resonators with different resonance frequencies. The remaining parts of this paper are as follows.

In Section 2, to evaluate the absorption characteristics of a perforated plate with various-sized holes and a porous separating partition, we developed the acoustic finite element (FE) simulation

method based on the Johnson-Champoux-Allard model (JCA model) [21–23] and the Beranek-Ingard model [21,24,25]. To consider the physical phenomenon around holes, we modified the tortuosity in the effective density formulation of the original JCA model and it is validated in connection with the end correction lengths around holes in the FE simulation environment.

In Section 3, using the developed FE simulation method, we investigated the absorption bandwidth-extending effect of using a porous separating partition between different sized holes. To reflect the material properties of a porous separating partition in the simulation, the Delany-Bazley material model is employed [26–28]. We compared the absorption coefficient graph of a perforated plate with a porous separating partition and that of a perforated plate with a rigid separating partition (under the same conditions) in two cases of two-sized-holes and four-sized holes, respectively.

In Section 4, based on the simulation results, we applied optimization techniques to the design problem of our new perforated plate model. So we optimized the hole sizes, flow resistivity value of porous separating partition and partition thickness to maximize the sum of absorption coefficients in a target frequency region. Finally, our findings and conclusions are summarized in Section 5.

## 2. Finite element analysis method for absorption performance of a perforated plate

Most previous research related to the absorption performance of perforated plates was conducted by theoretical analysis method and experiment. Thanks to the previous research, quite precise theoretical surface impedance models for a perforated plate have been developed. And the surface impedance can be used to calculate the absorption coefficient. Although there exist some papers that use theoretical approaches [5,7,8,12,17,29,30], it is not easy to derive the surface impedance when the structure behind the perforated plate becomes complex (like when the perforated plate has multiple hole sizes and a porous separating partition, as suggested by this paper). Therefore, we used a finite element method to effectively analyze the performance of the perforated plate suggested in this paper.

To reflect the absorption phenomena occurring in the holes of a perforated plate in FE simulation, we modified the effective density of the original Johnson-Champoux-Allard (JCA) model. The modified effective density substitutes the air density of holes in the present FE model. From [22], it was presented that the effective density of the JCA model can be used to derive surface impedance models of a perforated plate by considering the end correction length of hole for the tortuosity parameter. Although the Beranek-Ingard model was retrieved from the JCA model with some assumption in [22], we modified the JCA model so that the surface impedance by the JCA model is exactly same to the

Beranek-Ingard model in a theoretical perspective. It should be noted that there have not been any paper that used the modified effective density of the JCA model to the numerical simulation. However, the end correction lengths of the modified effective density should be corrected again in FE environment in order that the numerical simulation result is matched with that of the analytical solution.

### 2.1. Modification of the Johnson-Champoux-Allard model considering end correction effects

The three major noise absorbing mechanisms of a perforated plate are the resonance effect, the end correction effect, and the energy loss effect caused by viscous friction and heat transfer [24,31]. The resonance effect of a perforated plate is exactly the same as that of a Helmholtz resonator. In other words, air mass and air stiffness (originating from air bulk modulus) values inside of the small holes at the surface of a perforated plate cause local resonances, thereby causing acoustic energy absorption or noise attenuation. The end correction effect refers to the corrections of the hole length and the viscosity length caused by the local scattering of sound waves around holes. About the energy loss effect, because the energy loss due to heat transfer is so small, it can be neglected; this is not true for the energy loss by viscous friction with internal hole surfaces.

Acoustic FE simulation provides a reasonable solution for a complex perforated plate structure whose surface impedance is complex in its derivation. However, when assigning real air density value to a FE model of the Helmholtz's equation, only the resonance effect is simulated. The end correction effect is just simulated for the hole length not for the viscosity length. In order to consider the viscosity effect in a FE simulation, the effective density values of holes should be properly calculated. For example, the rigid frame porous model of the JCA model [21–23] was developed to simulate the noise attenuation effect of a perforated element [32–35]. Due to assumptions related to the geometry, this JCA model has typically been used for simplified geometries. In our acoustic simulation, the JCA model was used to calculate the effective density of holes of a perforated plate.

The effective density of the JCA model can be formulated as Eq. (1) [21,32]. Here,  $\rho_e$ ,  $\sigma_h$ ,  $\alpha_\infty$ , and  $\Lambda$  are the effective density, flow resistivity inside a cylindrical hole, tortuosity, and viscous characteristic length, respectively. For a cylindrical hole case, the tortuosity ( $\alpha_\infty$ ) becomes 1 and the viscous characteristic length ( $\Lambda$ ) becomes hole radius ( $r$ ). The density and viscosity of air are denoted by  $\rho (= 1.21 \text{ kg/m}^3)$  and  $\eta (= 1.5 \times 10^{-5} \text{ m}^2/\text{s})$ , respectively. For the perforated plate porosity,  $\phi (\phi = \pi r^2/A)$ ,  $A (A = d^2$  for evenly distributed holes) is the area of a perforated plate corresponding to one hole and  $d$  is the distance between adjacent holes. The perforated plate thickness or hole length is denoted by  $t_p$  and the air cavity thickness (depth) is denoted by  $t_a$ . Acoustic parameters are frequency of incident wave ( $f$ ), angular velocity of incident wave ( $\omega (= 2\pi f)$ ), speed of sound in air ( $c (= 343 \text{ m/s})$ ), and wave number of air ( $k (= \omega/c)$ ). Because the derivation of the JCA model is not the objective of this research, the JCA procedures are omitted; see [21–23] for more details about the JCA model.

$$\rho_e = \rho \alpha_\infty + \frac{\sigma_h \phi}{i\omega} \sqrt{1 + i \frac{4\omega \rho \alpha_\infty^2 \eta}{\sigma_h^2 \Lambda^2 \phi^2}} \quad (i = \sqrt{-1}), \quad \sigma_h = \frac{8\eta}{\phi r^2} \quad (1)$$

It is important to note that the original JCA formulas should be modified because the end correction effects caused by radiated wave and distorted flows around holes are not considered in the JCA model. The overall procedure of this section is illustrated in Fig. 2. To consider the end-effects in the JCA model, the tortuosity

values in Eq. (1) can be modified; the tortuosity values of the first term ( $\rho \alpha_\infty$ ) and the second term ( $(4\omega \rho \alpha_\infty^2 \eta)/(\sigma_h^2 \Lambda^2 \phi^2)$ ) can be modified. Compared the procedure presented in [22], we directly derived the tortuosity values so that the JCA model is exactly same with the Bernaek-Ingard model [21,24,25]. So the modified tortuosity values can be inversely computed in order that the theoretical surface impedance of an air-perforated plate-air-rigid wall system using the effective density in Eq. (2) is equal to that of the Bernaek-Ingard model in Eq. (3). In Eq. (3),  $Z'_s$  is the surface impedance of a perforated plate used in the Beranek-Ingard model. In the Beranek-Ingard model, the adjusted hole length (end correction length for hole length), added by the radiated wave, is denoted by  $\delta_1$  and the adjusted viscosity length (end correction length for viscosity), added by the distorted flow, is denoted by  $\delta_2$ . The two adjusted lengths ( $\delta_1$  and  $\delta_2$ ) are calculated by Eq. (3-2). By setting Eq. (2) equal to Eq. (3), the tortuosity values in Eq. (1) can be obtained as Eq. (4). Therefore the formulation for two end correction lengths of the Beranek-Ingard model in Eq. (3-2) can be considered in the effective density of the JCA model. After this procedure, the derived formula in Eq. (4) can be used to assign the effective density to the finite elements of holes.

$$\text{Effective impedance of the JCA model : } Z_s = i \frac{1}{\phi} \omega \rho_e t_p - i \rho c \cot(kt_a) \quad (2)$$

$$\begin{aligned} \text{Beranek - Ingard model : } Z'_s = & \frac{1}{\phi} \omega \rho \sqrt{\frac{2\eta}{\omega} \left( \frac{\delta_2}{r} + \frac{t_p}{r} \right)} \\ & + i \frac{1}{\phi} \omega \rho \left[ \sqrt{\frac{2\eta}{\omega} \left( \frac{\delta_2}{r} + \frac{t_p}{r} \right)} + t_p + \delta_1 \right] \\ & - i \rho c \cot(kt_a) \end{aligned} \quad (3-1)$$

$$\delta_1 = 1.7r \times \varepsilon(\phi) = 1.7r \times (1 - 1.47\sqrt{\phi} + 0.47\sqrt{\phi^3}), \delta_2 = 2r \quad (3-2)$$

$$\text{Tortuosity correction for the hole length : } \alpha_{\infty,1} = 1 + \frac{\delta_1}{t_p} \quad (4-1)$$

Tortuosity correction for the viscosity length :

$$\alpha_{\infty,2} = \sqrt{\rho \left( \frac{2r}{\delta_2} + \frac{2r}{t_p} \right)^2 + i \frac{16\eta}{\omega \rho r^2}} \quad (4-2)$$

$$\rho_e = \rho \alpha_{\infty,1} + \frac{\sigma_h \phi}{i\omega} \sqrt{1 + i \frac{4\omega \rho \alpha_{\infty,2}^2 \eta}{\sigma_h^2 \Lambda^2 \phi^2}} \quad (i = \sqrt{-1}) \quad (4-3)$$

But the absorption coefficient calculated by FE simulation using the theoretically modified effective density shows the discrepancy with that of the Beranek-Ingard model for the analysis of a simple perforate plate in Section 2.3. This discrepancy can be explained by the duplication of end correction of hole length both in the effective density and in the FE simulation, because radiation phenomenon around a hole is simulated in itself in FE simulation. So is desirable to make a further modification by setting  $\delta_1$  equal to 0. This is investigated in Section 2.3. In order to further improve the accuracy of the calculation, the adjusted hole length and the adjusted viscosity length can be corrected again by setting  $\delta_1 = C_1 r$ ,  $\delta_2 = C_2 r$  and determining the correction coefficients

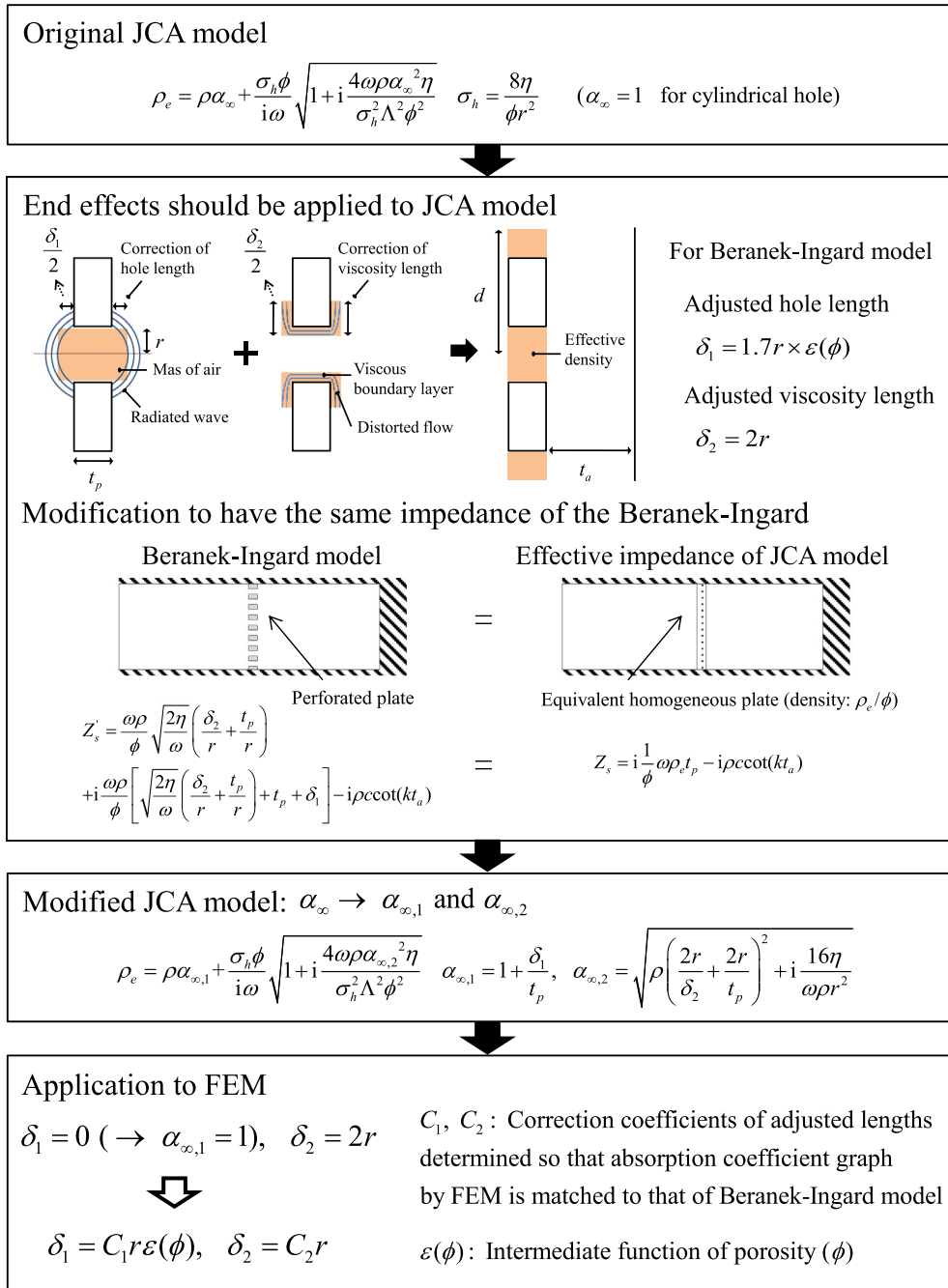


**Fig. 2.** Procedure for the modification of the JCA model. (The correction factors,  $\alpha_{\infty,1}$  and  $\alpha_{\infty,2}$  (tortuosity values) in the box are presented for the first time.)

( $C_1$  and  $C_2$ ). This is done such that the frequency at the peak point and the maximum absorption coefficient in the FE analysis are matched to those of the Beranek-Ingard solution.

## 2.2. Impedance tube modeling and calculation of absorption coefficient

In our FE simulation, considering the periodic arrangement of multiple holes, the inner volume of impedance tube which has square cross section and unit perforated plate as Fig. 3 can be computed by the Helmholtz equation. The weak formulation of the Helmholtz equation for FE analysis is given in Eq. (5) where  $p$  and  $\tilde{p}$  are acoustic pressure and virtual acoustic pressure in the acoustic domain,  $\Omega$ . The outward unit normal vector at the bound-

ary of the acoustic domain is  $\mathbf{n}$ . The sound hard wall boundary conditions as Eq. (6-1) are applied for all of the boundaries except for the inlet surface. The inlet surface is set to the plane wave radiation boundary condition with incident pressure ( $p_{in} = 1$  Pa) as Eq. (6-2). The material properties of air are assigned for all domains, except for the hole domain, and the effective density in Eq. (4-3) is assigned for the hole domain. The speed of sound in holes is set to that of air. The hole interval ( $d$ ) is set to 30 mm and the thickness values of the perforated plate and air cavity behind the perforated plate are set to 1 mm and 10 mm, respectively.

To calculate the absorption coefficient, the two-point pressure method (presented in Eq. (7) through Eq. (9)) is employed as Fig. 3c. Reflection coefficient, transfer function, acoustic pressure of incident wave, acoustic pressure of reflected wave, time, and

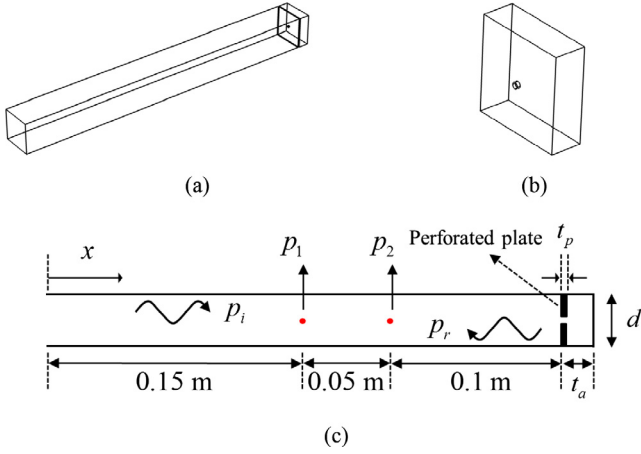


**Fig. 3.** Impedance tube modeling. (a) Modeling for the acoustic domain, (b) modeling for the unit perforated plate, and (c) the two-point method used to calculate the absorption coefficient.

displacement from the inlet surface are denoted as  $\gamma$ ,  $H_{21}$ ,  $p_i$ ,  $p_r$ ,  $t$ , and  $x$ , respectively. The acoustic pressure values  $p_1$  and  $p_2$  are measured at  $x_1 = 0.15$  m and  $x_2 = 0.2$  m, respectively.

$$\int \nabla \bar{p} \cdot \nabla p d\Omega - \frac{\omega^2}{c^2} \int \bar{p} p d\Omega = \int \bar{p} \nabla p \cdot \mathbf{n} d\Gamma \quad (5)$$

$$\nabla p \cdot \mathbf{n} = 0 \quad (6-1)$$

$$\nabla p \cdot \mathbf{n} = -i\frac{\omega}{c}p + 2i\frac{\omega}{c}p_{in} \quad (6-2)$$

$$p = p_i + p_r = (\hat{p}_i e^{-ikx} + \hat{p}_r e^{ikx}) e^{i\omega t} \quad (7)$$

$$\frac{p_2}{p_1} = \frac{\hat{p}_i e^{-ikx_2} + \hat{p}_r e^{ikx_2}}{\hat{p}_i e^{-ikx_1} + \hat{p}_r e^{ikx_1}} = \frac{e^{-ikx_2} + \gamma e^{ikx_2}}{e^{-ikx_1} + \gamma e^{ikx_1}} = H_{21} \quad \left( \gamma = \frac{\hat{p}_r}{\hat{p}_i} \right) \quad (8)$$

$$\gamma = \frac{H_{21} e^{-ikx_1} - e^{-ikx_2}}{e^{ikx_2} - H_{21} e^{ikx_1}}, \quad \alpha = 1 - |\gamma|^2 \quad (9)$$

### 2.3. Determination of end correction lengths of hole in FE environment

To check the accuracy of the modifications made in Eq. (4), we conducted a FE simulation for a perforated plate with a single hole size and no porous separating partition. The simulation result was compared with the theoretical absorption coefficient in Eq. (10), which was determined from the surface impedance of the Beranek-Ingard model in Eq. (3) [1,25]. In Fig. 4a, the result by the direct modification of the JCA model in Eq. (4) has the highest

absorption coefficient around 780 Hz, whereas the Beranek-Ingard model has the highest value at 1018 Hz. However, our modification, where the first tortuosity ( $\alpha_{\infty,1}$ ) was set to 1 ( $\delta_1 = 0$ ), significantly improves the prediction with the highest absorption value at 1040 Hz.

$$\alpha = \frac{4\text{Re}[Z'_s]/\rho c}{(\text{Re}[Z'_s]/\rho c + 1)^2 + (\text{Im}[Z'_s]/\rho c)^2} \quad (10)$$

When the adjusted lengths are set to  $\delta_1 = C_1 r$ ,  $\delta_2 = C_2 r$  as proposed in the Section 2.1,  $C_1 = 0.09$  and  $C_2 = 3$  show the best approximation as Fig. 4b. Table 1 shows the calculated values of the adjusted lengths and the corresponding values of  $\alpha_{\infty,1}$ ,  $\alpha_{\infty,2}$ , and  $\rho_e$ . Because  $\alpha_{\infty,2}$  and  $\rho_e$  are dependent on the frequency, it should be noted that the calculated values in Table 1 are for the frequency of 1000 Hz.

Furthermore, we observed that the appropriate value of two coefficients ( $C_1$  and  $C_2$ ) vary according to the hole radius. Table 2 shows frequencies at peak point and maximum absorption coefficients according to  $C_1$  and  $C_2$  for the three cases with different hole radius. It was observed that coefficient  $C_1$  tends to decrease the frequency at peak point as its value increases while also lowering the maximum absorption coefficient as its value increases.  $C_2$  tends to increase the frequency at peak point a little as its value increases while lowering the maximum absorption coefficient as its value increases.

Table 3 shows the values of  $C_1$  and  $C_2$  obtained for three different hole radii of 1.5 mm, 2 mm, and 2.5 mm. Then, we made second order interpolation functions of  $C_1$  and  $C_2$  with respect to the hole radius ( $r$ ) as Eq. (11). Then, new interpolated formulations of the two adjusted lengths ( $\delta_1$  and  $\delta_2$ ) can be obtained as Eq. (12).

$$C_1 = 100000r^2 - 470r + 0.63 \quad (11)$$

$$C_2 = 1000000r^2 - 2500r + 4 \quad r(\text{unit : m})$$

$$\delta_1 = C_1 r = (100000r^2 - 470r + 0.63)r \quad (12)$$

For the simulation, tetrahedral finite elements are used. To investigate the effect of mesh size, several mesh refinements were tested. For an example, Fig. 5 shows an example with the two mesh

**Table 1**

Calculated values of the adjusted lengths and the corresponding values of  $\alpha_{\infty,1}$ ,  $\alpha_{\infty,2}$ , and  $\rho_e$ . ( $\alpha_{\infty,1}$ ,  $\alpha_{\infty,2}$ , and  $\rho_e$  are calculated at 1000 Hz.)

$\delta_1 = 1.7r$ , $\delta_2 = 2r$	$\delta_1 = 0$ , $\delta_2 = 2r$	$\delta_1 = 0.09r$ , $\delta_2 = 3r$
$\delta_1 = 0.0028(2.8 \text{ mm})$	$\delta_1 = 0(0 \text{ mm})$	$\delta_1 = 0.00015(0.15 \text{ mm})$
$\delta_2 = 0.004(4 \text{ mm})$	$\delta_2 = 0.004(4 \text{ mm})$	$\delta_2 = 0.006(6 \text{ mm})$
$\alpha_{\infty,1} = 3.8121$	$\alpha_{\infty,1} = 1$	$\alpha_{\infty,1} = 1.1489$
$\alpha_{\infty,2} = 5.5 + 0.0007i$	$\alpha_{\infty,2} = 5.5 + 0.0007i$	$\alpha_{\infty,2} = 5.1333 + 0.0008i$
$\rho_e = 4.8216 - 0.2090i$	$\rho_e = 1.4190 - 0.2090i$	$\rho_e = 1.5852 - 0.1951i$

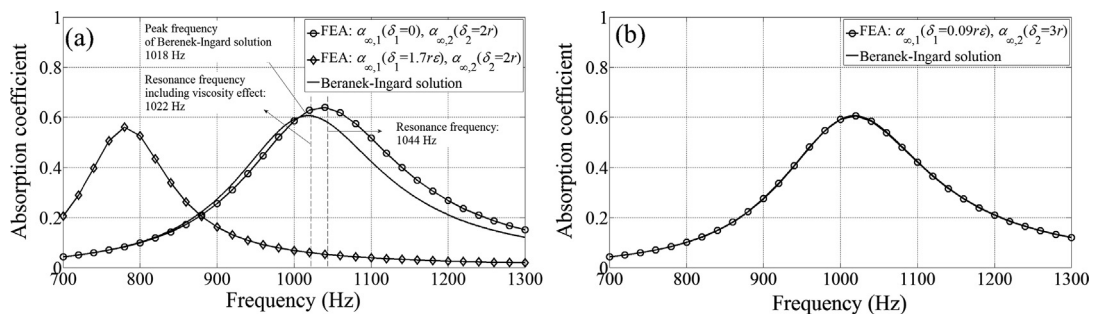


**Fig. 4.** FE analysis results compared with the analytical solution of the Beranek-Ingard model ( $t_p = 1$  mm,  $t_a = 10$  mm,  $d = 30$  mm, and  $r = 2$  mm). (a) FE result by the theoretical modification of the JCA model and (b) FE result by the further modification of the adjusted lengths.



**Table 2**

Peak frequencies and maximum absorption coefficients for different coefficients of adjusted lengths.

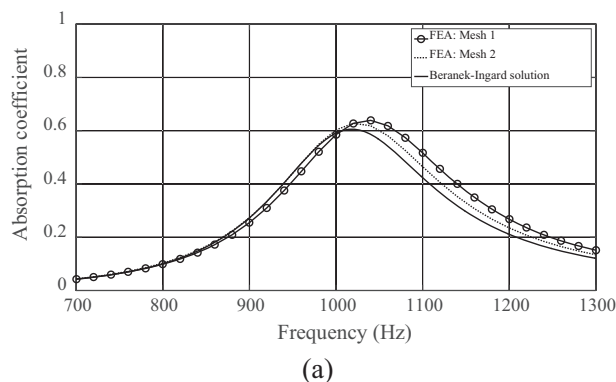
	$C_1 = 0.11$	$C_1 = 0.12$	$C_1 = 0.13$	$C_1 = 0.14$	$C_1 = 0.15$	$C_1 = 0.16$
<i>(a) <math>r = 1.5</math> mm <math>\delta_1 = C_1 r</math> <math>\delta_2 = C_2 r</math> (Beranek-Ingard solution: 825 Hz, 0.8076)</i>						
$C_2 = 2$	830 Hz, 0.8284	829 Hz, 0.8279	827 Hz, 0.8274	826 Hz, 0.8268	824 Hz, 0.8263	822 Hz, 0.8258
$C_2 = 2.5$	830 Hz, 0.8107	830 Hz, 0.8105	829 Hz, 0.8100	827 Hz, 0.8094	825 Hz, 0.8088	824 Hz, 0.8083
$C_2 = 3$	830 Hz, 0.7978	830 Hz, 0.7980	830 Hz, 0.7975	828 Hz, 0.7970	826 Hz, 0.7964	824 Hz, 0.7958
	$C_1 = 0.05$	$C_1 = 0.06$	$C_1 = 0.07$	$C_1 = 0.08$	$C_1 = 0.09$	$C_1 = 0.10$
<i>(b) <math>r = 2</math> mm <math>\delta_1 = C_1 r</math> <math>\delta_2 = C_2 r</math> (Beranek-Ingard solution: 1018 Hz, 0.6057)</i>						
$C_2 = 2.5$	1023 Hz, 0.6192	1023 Hz, 0.6187	1021 Hz, 0.6178	1019 Hz, 0.6170	1017 Hz, 0.6161	1014 Hz, 0.6153
$C_2 = 3$	1023 Hz, 0.6085	1023 Hz, 0.6081	1022 Hz, 0.6073	1020 Hz, 0.6065	1017 Hz, 0.6057	1015 Hz, 0.6048
$C_2 = 3.5$	1023 Hz, 0.6007	1023 Hz, 0.6004	1022 Hz, 0.5997	1020 Hz, 0.5988	1018 Hz, 0.5980	1016 Hz, 0.5972
	$C_1 = 0.05$	$C_1 = 0.06$	$C_1 = 0.07$	$C_1 = 0.08$	$C_1 = 0.09$	$C_1 = 0.10$
<i>(c) <math>r = 2.5</math> mm <math>\delta_1 = C_1 r</math> <math>\delta_2 = C_2 r</math> (Beranek-Ingard solution: 1198 Hz, 0.4588)</i>						
$C_2 = 3.5$	1203 Hz, 0.4660	1203 Hz, 0.4651	1200 Hz, 0.4642	1197 Hz, 0.4633	1194 Hz, 0.4624	1193 Hz, 0.4614
$C_2 = 4$	1203 Hz, 0.4616	1203 Hz, 0.4608	1200 Hz, 0.4599	1197 Hz, 0.4590	1194 Hz, 0.4581	1193 Hz, 0.4572
$C_2 = 4.5$	1203 Hz, 0.4582	1203 Hz, 0.4575	1200 Hz, 0.4565	1197 Hz, 0.4556	1195 Hz, 0.4538	1193 Hz, 0.4538

**Table 3**

Appropriate coefficient values of the adjusted lengths according to the hole radius.

	$r = 0.0015(1.5 \text{ mm})$	$r = 0.002(2 \text{ mm})$	$r = 0.0025(2.5 \text{ mm})$
$C_1$	0.15	0.09	0.08
$C_2$	2.5	3	4

sizes (Mesh 1 and Mesh 2: refined mesh than Mesh 1). In Fig. 5(a), the simulated absorption curve with Mesh 1 is same as that of Fig. 4(a) with  $\delta_1 = 0$ ,  $\delta_1 = 2r$ . With the refined mesh, the absorption curve becomes more closed to the Beranek-Ingard solution with some discrepancy. It implies that the two correction coefficients should be adjusted depending on the mesh size and the coefficient values can be used for the other frequency ranges. In the present study, the coefficients for the Mesh 1 are used for all the numerical simulations and the optimizations requiring a lot of iterative FE analyses. In our simulations, the wavelength  $\lambda (= c/f)$  varies from 0.26 m (for 1300 Hz) to 0.59 m (for 700 Hz). Therefore, the mesh densities in Fig. 5 are sufficiently small enough.



#### 2.4. Additional interpretation for a perforated plate with a single hole size

It is possible to interpret the impedance tube structure, shown in Fig. 3, as a Helmholtz resonator. For the example of Fig. 4, the generally-used resonance frequency calculated by Eq. (15) is 1044 Hz. However, the peak frequency by the Beranek-Ingard solution is 1018 Hz. Regarding this frequency error, it is important to recall that the generally-used resonance frequency formulation of the Helmholtz resonator does not include viscosity effect around necks, which correspond to the holes of a perforated plate. In this case, the Beranek-Ingard model can be used to calculate the resonance frequency that the viscosity effect is considered. The principle to derive this formulation is as follows. Resonance occurs when impedance is a real number with the same phase for particle velocity and pressure. Therefore, by setting the imaginary part of Eq. (3) equal to zero, some formulations like Eq. (13) can be obtained. Because Eq. (13) is the 4th order equation for  $\omega$ , four solutions of Eq. (14) exist for the example of Fig. 4. Considering that the peak

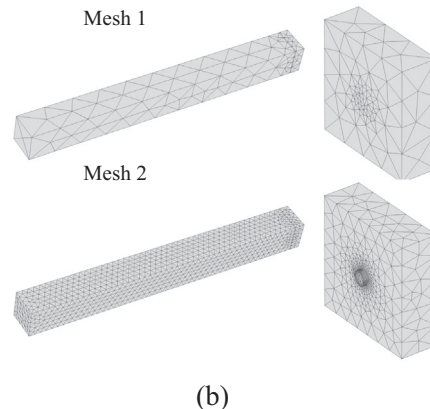


**Fig. 5.** (a) FE analysis results by  $\delta_1 = 0$ ,  $\delta_1 = 2r$  for the two mesh sizes and the minimum wavelength (0.26 m) and (b) the mesh figures (Mesh 1: maximum element size: 0.0311 (m) and Mesh 2: maximum element size: 0.0062 (m)).

frequency of the Beranek-Ingard model is 1018 Hz, we choose 1022 Hz as a resonance frequency considering the viscosity effect.

$$\frac{1}{\phi} \omega \left[ \sqrt{\frac{2\eta}{\omega}} \left( \frac{\delta_2}{r} + \frac{t_p}{r} \right) + t_p + \delta_1 \right] = c \cot(kt_a) \cong \frac{c}{kt_a} = \frac{c^2}{\omega t_a}$$

$$\rightarrow \omega^2 \left[ \sqrt{\frac{2\eta}{\omega}} \left( \frac{\delta_2}{r} + \frac{t_p}{r} \right) + t_p + \delta_1 \right] = \frac{c^2 \phi}{t_a} \quad (13)$$

$$f = \omega_{sol}/2\pi$$

$$= 1022.1, 1068.4, -1044.3 + 23.150i, -1044.3 - 23.150i \quad (14)$$

By deleting the viscosity term in Eq. (13), we can obtain the generally-used formulation of the Helmholtz resonance frequency as Eq. (15).

$$\omega^2 [t_p + \delta_1] = \frac{c^2 \phi}{t_a} \rightarrow \omega = c \sqrt{\frac{\phi}{t_a(t_p + \delta_1)}} \quad (15-1)$$

$$f = \omega/2\pi = 1044.8 \quad (15-2)$$

In the numerical example of Fig. 4, only on unit cell having a single hole was considered for a perforated plate with uniformly repeated hole pattern. In order to test the validity of this assumption and to show the effect of separating holes by the rigid separators, analysis for the four unit cells (with and without rigid separators) was conducted. As Fig. 6b, the same absorption coefficient response was obtained for the three comparison models shown in Fig. 6a. For the four unit cells without rigid separators, it is interesting that the acoustic pressure caused by air oscillation at the middle locations between two adjacent holes acts as if rigid

separator exists. Here, the rigid separator is modeled by the interior hard wall condition assuming that the rigid separator is very thin.

### 3. Absorption bandwidth-extending effect of a porous separating partition

To enhance the performance of a perforated plate, this section introduces a porous separating partition. And hole sizes, thickness of separating partition and material property of porous partition are varied. Without a loss of generality, in order to investigate the basic performance of a perforated plate, we consider the existence of holes with two or four different radii.

#### 3.1. Absorption performance of a porous layer (Delany-Bazley empirical model) without a perforated plate

One of the most common approaches to reduce noise is to place a porous layer on a rigid wall [10]. In order to illustrate the basic absorption performance of a porous layer without a front perforated plate, the pressure attenuation performance of an 11-mm-thick porous layer was calculated in Fig. 7. The pressure attenuation characteristics of the porous layer are numerically modeled by the Delany-Bazley empirical model. The Delany-Bazley empirical model represents the acoustic characteristics of a fibrous material based on experimental data according to the frequency and flow resistivity value. In Fig. 7b, above 2000 Hz, the porous layer shows absorption coefficients over 0.5; however, the absorption coefficients below 2000 Hz are reduced under 0.5. Therefore, the porous layer configuration shown in Fig. 7a is effective for higher frequency ranges.

The basic formulas of the Delany-Bazley empirical model is as Eqs. (16)–(19). Here, density, speed of sound, and flow resistivity

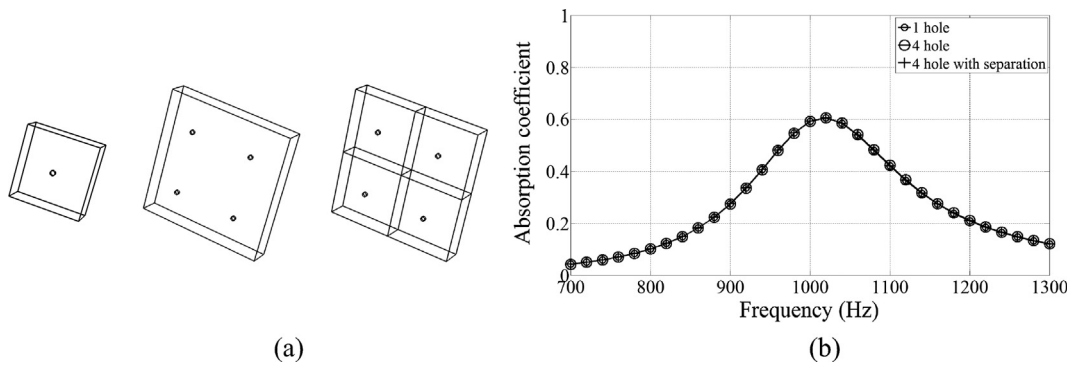


Fig. 6. Analysis results for the perforated plates with four unit cell. (a) Three perforated plate geometries used for comparison and (b) their absorption coefficient graphs.

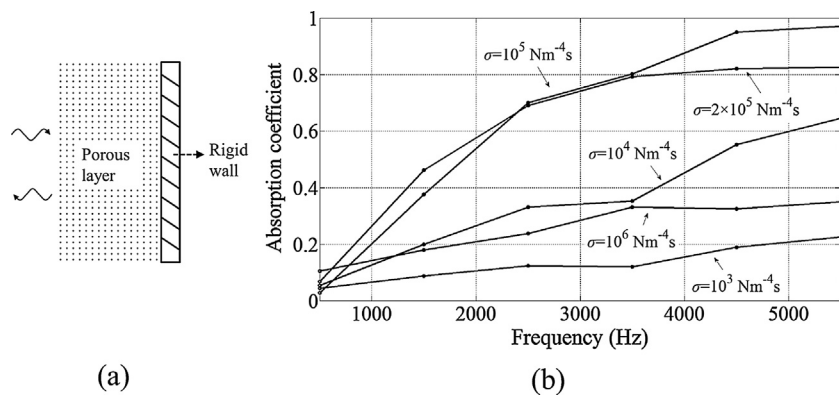


Fig. 7. Absorption performance of a porous layer. (a) Porous layer without a perforated plate and (b) absorption coefficient graphs with some flow resistivity values.

of porous material are denoted as  $\rho_{\text{porous}}$ ,  $c_{\text{porous}}$ , and  $\sigma$ , respectively. Wave number and characteristic impedance of a porous material are denoted as  $k_{\text{porous}}$  and  $z_{\text{porous}}$ , respectively. In the original paper that presented the Delany-Bazley empirical model [26], it was mentioned that the frequency and flow resistivity value are effective in the region shown in Eq. (19). Therefore, the Delany-Bazley model, the Miki's model in [36], and recent improvements made in [37] are all effective within this range. In our research, flow resistivity values beyond this effective region are also used for a parametric study. However, in [26], the value of  $\rho f / \sigma$  was measured to be as high as 0.001 and the flow resistivity value was measured to be as high as  $10^6 \text{ N m}^{-4} \text{ s}$ . For this reason, permitting to extend the effective range of  $\rho f / \sigma$  to 0.001, we use a flow resistivity value as high as  $10^6 \text{ N m}^{-4} \text{ s}$  around 1000 Hz.

$$k_{\text{porous}} = k \left( 1 + 0.0978 \left( \frac{\rho f}{\sigma} \right)^{-0.7} - i 0.189 \left( \frac{\rho f}{\sigma} \right)^{-0.595} \right) \quad (16)$$

$$z_{\text{porous}} = \rho c \left( 1 + 0.0571 \left( \frac{\rho f}{\sigma} \right)^{-0.734} - i 0.087 \left( \frac{\rho f}{\sigma} \right)^{-0.732} \right) \quad (17)$$

$$f = \frac{\omega}{2\pi}, \quad \rho_{\text{porous}} = z_{\text{porous}} \times k_{\text{porous}} / \omega, \quad c_{\text{porous}} = \frac{\omega}{k_{\text{porous}}} \quad (18)$$

$$0.01 < \frac{\rho f}{\sigma} < 1.0 \quad (19)$$

### 3.2. Absorption performance of a perforated plate with two-sized holes and effect of a porous separating partition

While a porous material layer is effective for higher frequency ranges as illustrated in Section 3.1, a perforated plate can be used to improve the pressure attenuation performance at low frequency ranges. To illustrate its advantages at low frequency ranges, Fig. 8 shows the absorption coefficient graphs of three types of perforated plates with two-sized holes:  $r_1$  and  $r_2$ . Without a loss of generality, the radii of holes are varied between 1.8 mm and 2.2 mm.

Fig. 8a shows the perforated plate with the two-sized holes and no separating partition. For perforated plates with identically-sized holes, larger hole sizes lead to higher peak frequencies. It is interesting that the peak frequency of the perforated plate with 1.8 mm and 2.2 mm for  $r_1$  and  $r_2$  is same as that of the perforated plate

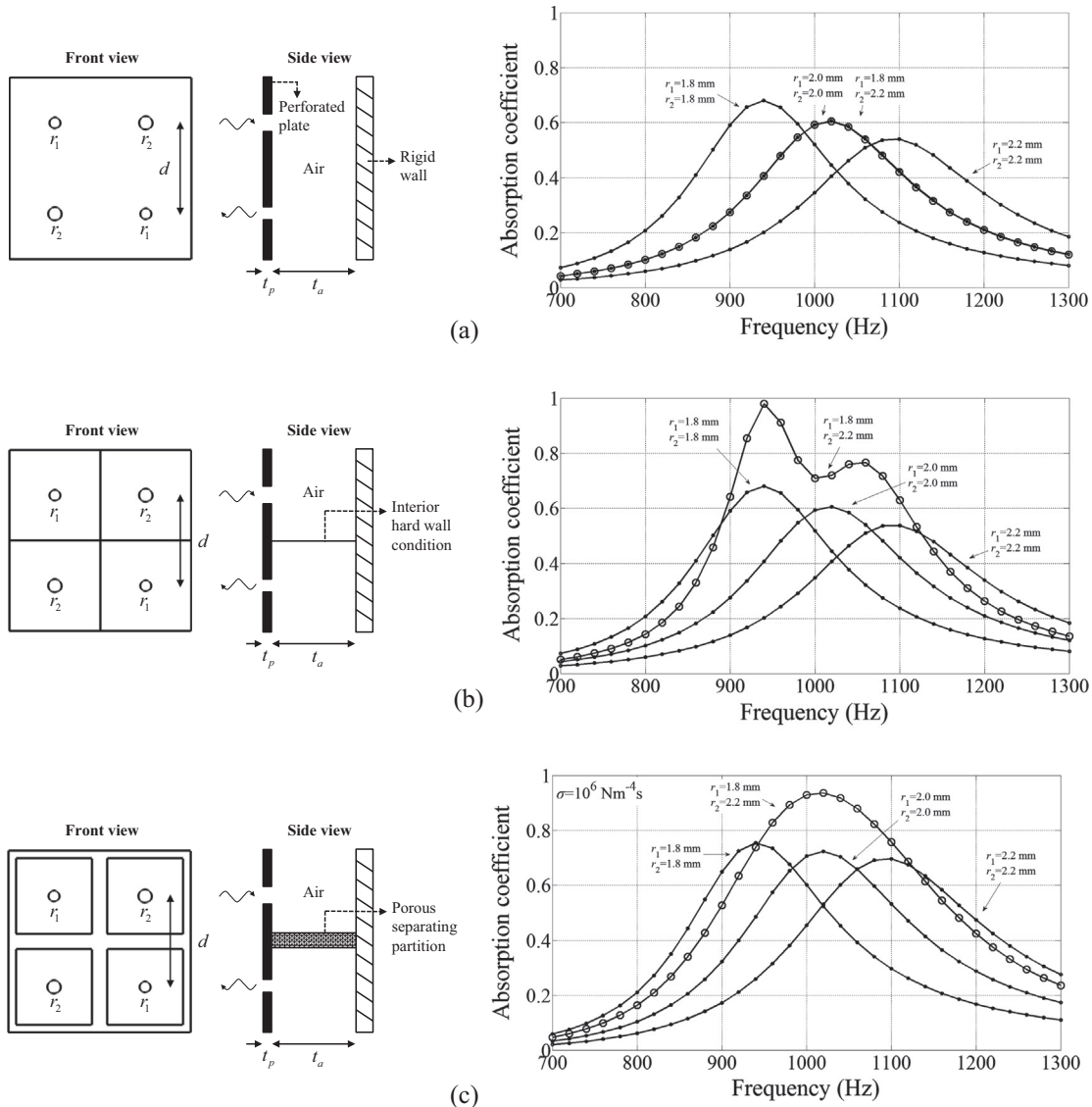


**Fig. 8.** Analysis of a perforated plate with two hole sizes ( $t_p = 1 \text{ mm}$ ,  $t_a = 10 \text{ mm}$ ,  $d = 30 \text{ mm}$ ,  $r_1 = 1.8 \text{ mm}$ , and  $r_2 = 2.2 \text{ mm}$ ). (a) Not-separated air cavity, (b) air cavity separated by a rigid partition (interior hard wall boundary), and (c) air cavity separated by a porous partition (thickness of 5 mm).



with a single hole size of 2 mm (radius). This phenomenon occurs because the effective acoustic mass and the effective acoustic stiffness of the perforated plate with two hole sizes of 1.8 mm and 2.2 mm are same as those of the perforated plate with single hole size of 2 mm.

However, when the space behind the perforated plate is equally separated by using the interior hard wall boundary condition, as shown in Fig. 8b, two peaks appear because there are two different Helmholtz resonators. Because the effective mass and stiffness values of the separated internal spaces are equal to those of the cavities with a single hole size of 1.8 and 2.2 mm (radius), the peak frequencies are located close to those of the perforated plate with 1.8 mm hole and the perforated plate with 2.2 mm hole. The amplitude of the absorption coefficient at peak frequencies becomes higher by combining two different hole sizes. However, this is not a general phenomenon, and the absorption coefficient at peak frequencies can become lower for other perforated plate sizes.

In order to improve the pressure attenuation performance in a wide-band frequency region, the present study now employs a porous separating partition with a thickness ( $t_{pa}$ ) of 5 mm, as shown Fig. 8c. It is our proposition that intermediate characteristics, between the characteristics of a perforated plate with no partition and the characteristics of a perforated plate with a rigid partition, can be achieved by employing a semi-rigid porous material. Fig. 8c shows the pressure attention with a porous separating partition that has a flow resistivity of  $10^6 \text{ N m}^{-4} \text{ s}$ . Unlike the configuration that includes a rigid wall, the installation of this porous separating partition causes some major changes in the absorption coefficient graph; the frequency region of the high absorption coefficient becomes wider without peak frequencies corresponding to each hole size.

Fig. 9a compares the absorption coefficients of the perforated plate with a porous separator and the perforated plate with a rigid separator. Because the porous separator permits air flow, it is not a rigid wall and the absorption coefficient curve becomes smoother. Compared with the rigid separator, it has a wider frequency region where the absorption coefficient is high. Interestingly, with a flow resistivity value of  $2 \times 10^6$ , the frequency region of high absorption coefficient becomes much larger compared to a flow resistivity value of  $10^6$ . Fig. 9b shows the absorption coefficient graphs of perforated plates with porous separating partitions of various thicknesses. As the thickness value is increased to 7 mm, the absorption coefficient becomes higher over the entire frequency region. When the thickness value is set to 9 mm, the absorption coefficient near the peak frequency becomes slightly lower while the absorption coefficient in the remaining frequency region increases.

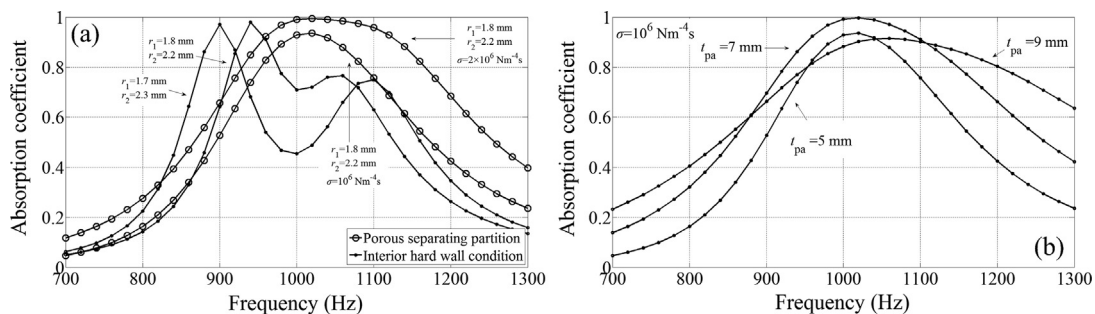


Fig. 9. (a) Comparison between the porous separating partition and the interior hard wall condition and (b) absorption coefficient graphs with various thickness values of the porous separating partition.

### 3.3. Absorption performance of a perforated plate with four-sized holes and effect of a porous separating partition

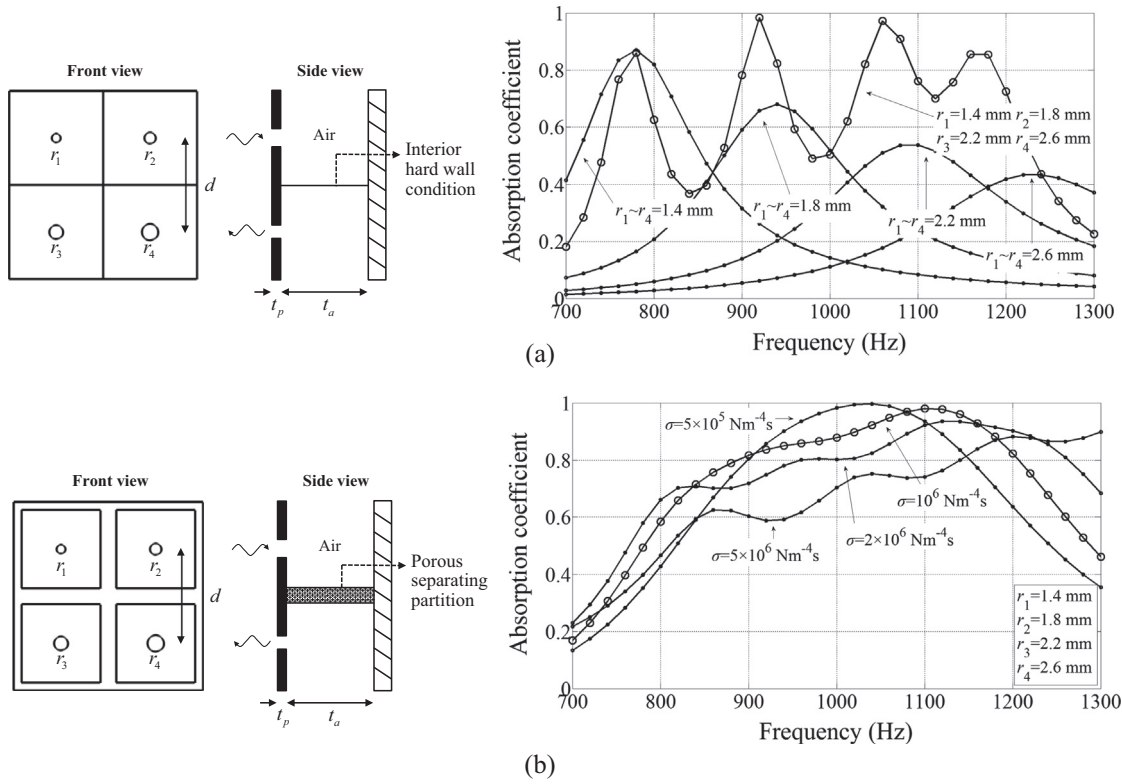
In this section, a perforated plate with four-sized holes is investigated. All of the geometric configurations are the same as those used in the previous sections ( $t_p = 1 \text{ mm}$ ,  $t_a = 10 \text{ mm}$ , and  $d = 30 \text{ mm}$ ). Considering the effective mass and stiffness values, the sizes of four holes ( $r_1$ ,  $r_2$ ,  $r_3$ , and  $r_4$ ) are set to 1.4 mm, 1.8 mm, 2.2 mm, and 2.6 mm, respectively, in order to have peak frequencies between 700 Hz and 1300 Hz. Fig. 10(a) and (b) shows the absorption coefficient curves with the interior hard wall condition and the porous separating partition condition, respectively. As expected, with the interior hard wall condition, each box has different resonance frequencies, which appear in the curve. However, with the porous separating partition, four interior spaces work as one box and four resonance frequencies are not clearly distinguished. The porous separating partition causes the graph of the interior hard wall condition to be smoother. Additionally, the absorption coefficient graph depicts continuous high absorption performance over a wide frequency region.

Fig. 11 shows the absorption coefficients for different thickness values of the porous partition of Fig. 10b. According to the thickness and flow resistivity value of the porous partition, the absorption coefficient graph changes. Therefore, it should be possible to apply some structural optimization techniques to improve the pressure attenuation performance of a perforated plate.

### 4. Wide-band absorption performance optimization of a perforated plate

The previous section showed that a perforated plate with different sized holes and a porous separating partition can provide better pressure attenuation compared to the conventional Helmholtz resonators. However it is difficult to find out intuitively some geometrical parameters such as the sizes of holes, the thicknesses of internal porous separator to improve the absorption performance. Therefore we propose to apply the numerical optimization technique to find out optimal geometrical configurations of a perforated plate with multiple-sized holes and a porous separating partition. The finite element approach is used for the forward analysis and the finite difference method is used for the sensitivity analysis. The sequential quadratic programming (SQP) approach is used for the optimization algorithm. The SQP method is one of established optimization algorithms [38]. The SQP algorithm solves the QP problem in Eq. (20) for the search direction,  $\mathbf{d}$ .

$$\begin{aligned} & \text{Min } \nabla \mathbf{f}(\mathbf{x})^T \mathbf{d} + \frac{1}{2} \mathbf{d}^T \mathbf{H} \mathbf{d} \\ & \text{Subject to } \nabla \mathbf{g}_j(\mathbf{x})^T \mathbf{d} + \mathbf{g}_j(\mathbf{x}) \leq 0, j = 1, \dots, m \\ & \nabla \mathbf{h}_k(\mathbf{x})^T \mathbf{d} + \mathbf{h}_k(\mathbf{x}) = 0, k = 1, \dots, l \end{aligned} \quad (20)$$



**Fig. 10.** Analysis of a perforated plate with four hole sizes ( $t_p = 1$  mm,  $t_a = 10$  mm,  $d = 30$  mm,  $r_1 = 1.4$  mm,  $r_2 = 1.8$  mm,  $r_3 = 2.2$  mm, and  $r_4 = 2.6$  mm). (a) Interior hard wall boundary condition and (b) porous separating partition (thickness of 5 mm).

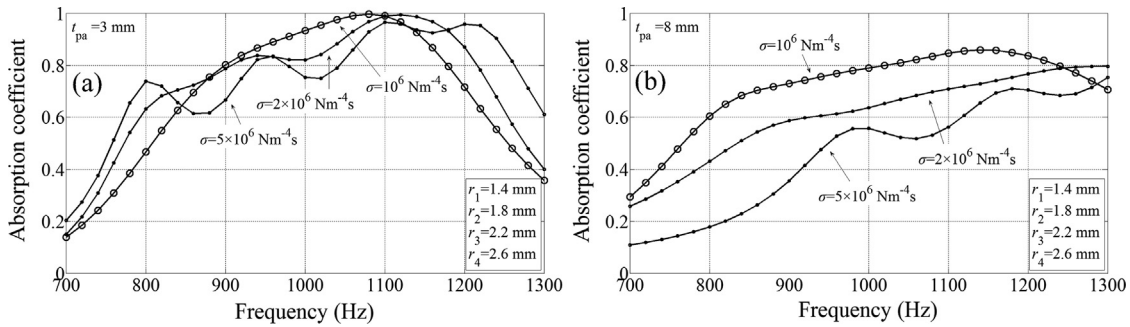


**Fig. 11.** Absorption coefficient graphs with various flow resistivity values of the porous separating partition for the thicknesses of (a) 3 mm and (b) 8 mm.

where the gradients of the objective function and the  $j$ -th equality and the  $k$ -th inequality constraints are denoted by  $\nabla f$ ,  $\nabla g_j$  and  $\nabla h_k$ . The Hessian of the objective function is  $\mathbf{H}$  which is computed by BFGS algorithm. The design variables are  $\mathbf{x}$ . In the present study, the optimization toolbox in MATLAB is used.

#### 4.1. Optimization of a perforated plate with interior hard wall condition

First of all, the sizes of holes of a perforated plate with interior hard wall are optimized. The optimization formulation is set to as Eq. (21). The object summing the absorption coefficients,  $\alpha_f$ , at the frequency range of interest is denoted by  $obj$ . We tried to improve the absorption performance in the frequency range from 700 Hz to 1300 Hz. In this optimization example, the predetermined minimum hole radius is set to 1.2 mm and the maximum hole radius is set to 2.8 mm. Considering the frequency range, we manually set the hole radii of 1.4 mm, 1.8 mm, 2.2 mm and 2.6 mm as an ini-

tial design. The finite different method is applied for the sensitivity analysis with the 0.05 mm for the design variable intervals.

$$\begin{aligned} \text{Max } obj(\mathbf{x}) &= \sum \alpha_f f = 700, 720, \dots, 1280, 1300 \text{ (Hz)} \\ \text{subject to } r_1 &\leq r_2 \leq r_3 \leq r_4 \text{ (mm)} \\ \mathbf{x} &= [r_1 r_2 r_3 r_4] (1.2 \leq r_i \leq 2.8, i = 1, 2, 3, \text{ and } 4) \end{aligned} \quad (21)$$

Table 4 shows the optimization results for the formulation of Eq. (21). After the optimization, the objective function was improved a little from 18.9101 to 19.1046. As shown in Fig. 12, the absorption coefficient graph obtained by the optimization process does not represent evidently improved effect.

**Table 4**  
Optimization result for the design variables of hole sizes.

Initial values	$\mathbf{x}_{\text{initial}} = [1.4000 \ 1.8000 \ 2.2000 \ 2.6000]$	$obj_{\text{initial}} = 18.9101$
Optimum values	$\mathbf{x}_{\text{optimized}} = [1.3531 \ 1.6594 \ 2.0837 \ 2.6469]$	$obj_{\text{optimized}} = 19.1046$

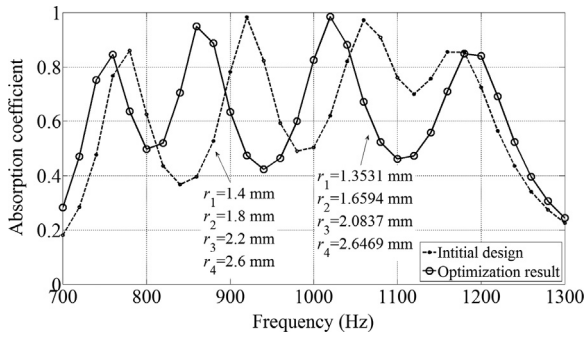


Fig. 12. Absorption coefficient curves before and after optimization for Table 4.

#### 4.2. Optimization of a perforated plate with a porous separating partition

In this subsection, absorption performance of a perforated plate with a porous separating partition is optimized. With the porous separating partition, it is possible to obtain absorption characteristics which are hard to be obtained by adjusting the sizes of holes for the interior hard wall condition. So, the thickness and the flow resistance value of the porous separating partition are added as two additional design variables.

First with the fixed 5 mm thickness of the porous separating partition, the flow resistivity value is optimized along with four hole radii. Optimization formulation is set to as Eq. (22) and Table 5a shows the optimized values. In Fig. 13a, frequency region with absorption coefficient above 0.75 became wider after the optimization.

$$\begin{aligned} \text{Max } obj(\mathbf{x}) &= \sum \alpha_{ff} = 700, 720, \dots, 1280, 1300 \text{ (Hz)} \\ \text{Subject to } r_1 &\leq r_2 \leq r_3 \leq r_4 \text{ (mm)} \\ 10^5 &\leq \sigma \leq 10^7 \text{ (N m}^{-4} \text{ s)} \\ \mathbf{x} &= [r_1 r_2 r_3 r_4, \sigma] (1.2 \leq r_i \leq 2.8, i = 1, 2, 3, \text{ and } 4) \end{aligned} \quad (22)$$

Table 5

(a) Optimization result for the design variables of hole sizes and flow resistivity value.  
(b) Optimization result for the design variables of hole sizes, flow resistivity value and thickness.

(a)	
Initial values	$\mathbf{x}_{\text{initial}} = [1.4000 \ 1.8000 \ 2.2000 \ 2.6000 \ 10^6] \text{ } obj_{\text{initial}} = 22.5261$
Optimum values	$\mathbf{x}_{\text{optimized}} = [1.2492 \ 1.5000 \ 2.1116 \ 2.7172 \ 7.53 \times 10^5] \text{ } obj_{\text{optimized}} = 23.4765$
(b)	
Initial values	$\mathbf{x}_{\text{initial}} = [1.4000 \ 1.8000 \ 2.2000 \ 2.6000 \ 10^6 \ 5] \text{ } obj_{\text{initial}} = 22.5261$
Optimum values	$\mathbf{x}_{\text{optimized}} = [1.2519 \ 1.5250 \ 1.9630 \ 2.7926 \ 2.549 \times 10^6 \ 1.540] \text{ } obj_{\text{optimized}} = 24.0098$

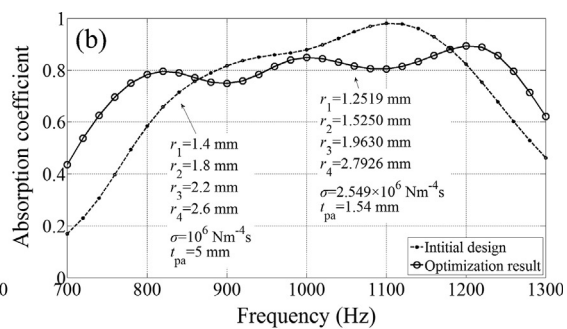
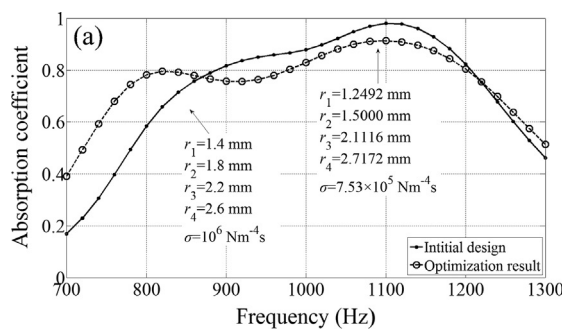


Fig. 13. Absorption coefficient curves before and after optimization (a) for Table 5(a) and (b) for Table 5(b).

Then the thickness of the porous separating partition is added to the optimization problem as Eq. (23). The optimized values are given in Table 5b. By adding the thickness to the design variable, the object function was improved from 22.5261 to 24.0098. So it shows the potential of the present approach. For the optimized curve in Fig. 13b, frequency region with absorption coefficient above 0.75 became wider than that of Fig. 13a.

$$\begin{aligned} \text{Max } obj(\mathbf{x}) &= \sum \alpha_{ff} = 700, 720, \dots, 1280, 1300 \text{ (Hz)} \\ \text{Subject to } r_1 &\leq r_2 \leq r_3 \leq r_4 \text{ (mm)} \\ 10^5 &\leq \sigma \leq 10^7 \text{ (N m}^{-4} \text{ s)}, 1 \leq t_{pa} \leq 10 \text{ (mm)} \\ \mathbf{x} &= [r_1 r_2 r_3 r_4, \sigma, t_{pa}] (1.2 \leq r_i \leq 2.8, i = 1, 2, 3, \text{ and } 4) \end{aligned} \quad (23)$$

#### 4.3. Optimization for a different target frequency region

In the previous examples, the object of optimization was to maximize the sum of absorption coefficients in the frequency range from 700 Hz to 1300 Hz. In this subsection, we conducted optimization that maximizes the absorption performance in more narrow frequency region than that of previous examples. Optimization formulations are same with those of previous examples except the frequency region of the object function. One frequency region is from 800 Hz to 1200 Hz and the other frequency region is from 900 Hz to 1100 Hz. For two cases, the object function values to maximize are expressed as Eq. (24):

$$\text{Max } obj(\mathbf{x}) = \sum \alpha_{ff} = 800, 820, \dots, 1180, 1200 \text{ (Hz)} \quad (24-1)$$

$$\text{Max } obj(\mathbf{x}) = \sum \alpha_{ff} = 900, 920, \dots, 1080, 1100 \text{ (Hz)} \quad (24-2)$$

Table 6 and Fig. 14 are optimization results for the perforated plate with interior hard wall condition. The design variables are radii of four holes. When the target frequency region is from 900 Hz to 1100 Hz, the optimized absorption coefficient graph of Fig. 14b shows flat graph-line in high absorption coefficient region without fluctuation which is seen in the optimized absorption curve of Fig. 14a.

Table 7 and Fig. 15 are optimization results for the perforated plate with a porous separating partition. The design variables are

Table 6

Optimization result for the design variables of hole sizes.

800–1200 Hz	Initial values	$\mathbf{x}_{\text{initial}} = [1.4000 \ 1.8000 \ 2.2000 \ 2.6000] \text{ } obj_{\text{initial}} = 14.5006$
	Optimum values	$\mathbf{x}_{\text{optimized}} = [1.5449 \ 10.7407 \ 20.0317 \ 2.4237] \text{ } obj_{\text{optimized}} = 16.0952$
900–1100 Hz	Initial values	$\mathbf{x}_{\text{initial}} = [1.4000 \ 1.8000 \ 2.2000 \ 2.6000] \text{ } obj_{\text{initial}} = 8.2584$
	Optimum values	$\mathbf{x}_{\text{optimized}} = [1.7866 \ 1.7866 \ 1.9419 \ 2.2101] \text{ } obj_{\text{optimized}} = 9.5842$

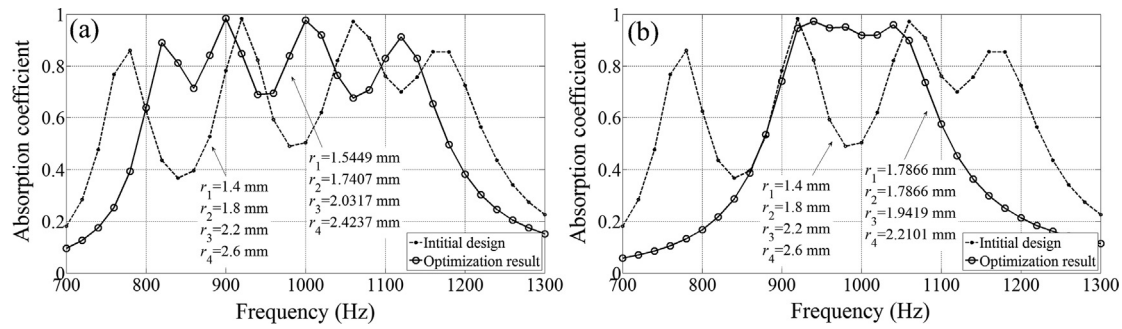


Fig. 14. Absorption coefficient curves before and after optimization for Table 6. Target frequency range of (a) 800–1200 Hz and (b) 900–1100 Hz.

Table 7

Optimization result for the design variables of hole sizes and flow resistivity value.

800–1200 Hz	Initial values	$\mathbf{x}_{\text{initial}} = [1.4000 \ 1.8000 \ 2.2000 \ 2.6000 \ 10^6]$	$\text{obj}_{\text{initial}} = 17.9064$
	Optimum values	$\mathbf{x}_{\text{optimized}} = [1.4137 \ 10.6546 \ 20.1256 \ 2.6118 \ 6.42 \times 10^5]$	$\text{obj}_{\text{optimized}} = 18.0700$
900–1100 Hz	Initial values	$\mathbf{x}_{\text{initial}} = [1.4000 \ 1.8000 \ 2.2000 \ 2.6000 \ 10^6]$	$\text{obj}_{\text{initial}} = 90.8270$
	Optimum values	$\mathbf{x}_{\text{optimized}} = [1.4453 \ 10.6964 \ 20.2065 \ 20.4849 \ 5.24 \times 10^5]$	$\text{obj}_{\text{optimized}} = 10.4230$

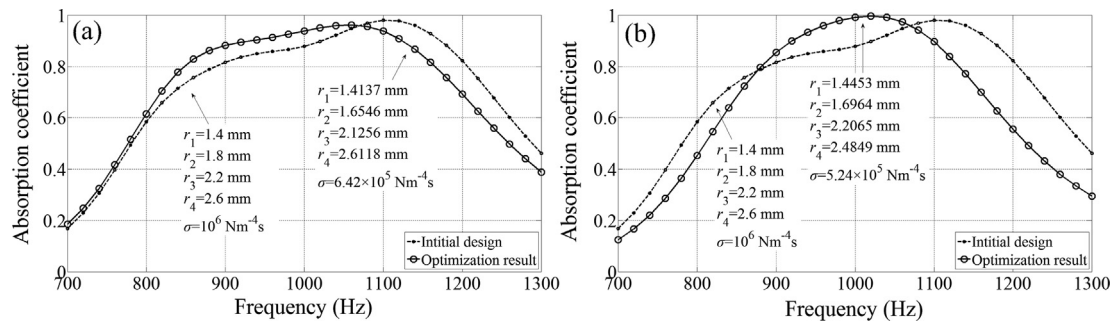


Fig. 15. Absorption coefficient curves before and after optimization for Table 7. Target frequency range of (a) 800–1200 Hz and (b) 900–1100 Hz.

Table 8

Optimization result for the design variables of hole sizes, flow resistivity value and thickness.

800–1200 Hz	Initial values	$\mathbf{x}_{\text{initial}} = [1.4000 \ 1.8000 \ 2.2000 \ 2.6000 \ 10^5]$	$\text{obj}_{\text{initial}} = 170.9064$
	Optimum values	$\mathbf{x}_{\text{optimized}} = [1.3652 \ 1.6597 \ 1.9679 \ 20.6131 \ 90.60 \times 10^5 \ 3.944]$	$\text{obj}_{\text{optimized}} = 18.1600$
900–1100 Hz	Initial values	$\mathbf{x}_{\text{initial}} = [1.4000 \ 1.8000 \ 2.2000 \ 2.6000 \ 10^5]$	$\text{obj}_{\text{initial}} = 9.8270$
	Optimum values	$\mathbf{x}_{\text{optimized}} = [1.5629 \ 10.7105 \ 20.0928 \ 20.5715 \ 40.32 \times 10^5 \ 60.162]$	$\text{obj}_{\text{optimized}} = 10.3717$

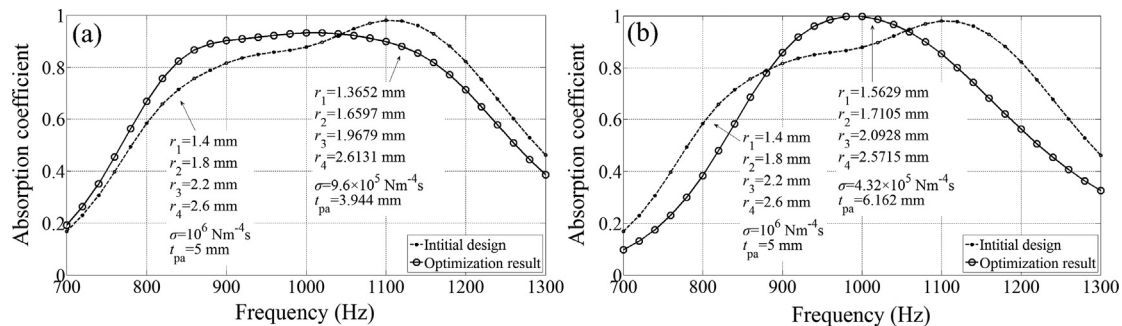


Fig. 16. Absorption coefficient curves before and after optimization for Table 8. Target frequency range of (a) 800–1200 Hz and (b) 900–1100 Hz.

radii of four holes and flow resistivity value. When the target frequency region is from 900 Hz to 1100 Hz, the object function value shows some increase and the optimized absorption coefficient

curve in Fig. 15b shows high absorption performance in the target frequency region. But the increase of object function value is small when the target frequency region is from 800 Hz to 1200 Hz.



Table 8 and Fig. 16 are optimization results when the thickness of porous partition is added to the design variables. Contrast to the result in previous subsection, adding the thickness to design variables is not so effective in maximizing the objection function value. This can be understood by the concept of local optimum solution. Also the optimized absorption coefficient graphs in Figs. 15 and 16 are similar.

## 5. Conclusion

The present study can be summarized by two important topics. The first topic is to present a novel configuration of a perforated plate with multiple-sized holes and a porous separating partition to achieve wide-band frequency absorption performance. The second topic is to construct acoustic FE model for the noise attenuation of a perforated plate by deriving the effective density of hole that includes the end correction effect and the energy loss effect caused by viscous friction.

We proposed an effective acoustic FE simulation method based on applying the Johnson-Champoux-Allard model to the hole air density. To apply the JCA model to the FE simulation correctly, investigation into the adjusted hole length and the adjusted viscosity length was conducted. Finally, some interpolation functions with respect to the hole radius were proposed for the coefficients of the adjust lengths. After that, we proposed a combination effect that utilizes multiple hole sizes (two hole sizes and four hole sizes). To obtain high absorption performance over a wide frequency region by using multiple sized-holes, the air cavity behind the perforated plate should be separated by either a rigid partition (interior hard wall condition) or a porous partition with high flow resistivity. Compared to the rigid partition, the porous partition can obtain some continuous frequency regions with high absorption coefficients. Some analyses with different flow resistivity values and thicknesses of the porous partition were conducted. After the development for effective acoustic FE model, mathematical optimization method was used to design the perforated plate with a porous separating partition which has better wide-band frequency absorption performance. So the sizes of four holes, flow resistivity value and thickness of porous partition were optimized. Optimization was also conducted for different target frequency ranges.

In conclusion, this paper presents appropriate analysis and optimization approach method for a perforated plate with multiple-sized holes and a porous separating partition which is devised for noise attenuation in a wide frequency region. As a result, we expect that the proposed perforated plate system can be utilized as a good alternative to extend the frequency region of high absorption coefficient.

## Acknowledgements

This research is funded by the human resources program in energy technology of the Korea Institute of Energy Technology Evaluation and Planning (KETEP), granted financial resource from the Ministry of Trade, Industry & Energy, Republic of Korea (No. 20154030200900) and the Global Frontier R&D Program on Center for Wave Energy Control based on Metamaterials funded by the National Research Foundation under the Ministry of Science, ICT & Future Planning, Korea (No. 2014M3A6B3063711).

## References

- [1] Lee FC, Chen WH. Acoustic transmission analysis of multi-layer absorbers. *J Sound Vib* 2001;248:621–34.
- [2] Miasa IM, Okuma M. Theoretical and experimental study on sound absorption of a multi-leaf microperforated panel. *J Syst Design Dynamics* 2007;1:63–72.
- [3] Zhang ZM, Gu XT. The theoretical and application study on a double layer microperforated sound absorption structure. *J Sound Vib* 1998;215:399–405.
- [4] Sakagami K, Morimoto M, Yairi M. Recent developments in applications of micro perforated panel absorbers. In: 14th International congress on sound and vibration, Australia; 2007.
- [5] Tao Z, Zhang B, Herrin DW, Seybert AF. Prediction of sound-absorbing performance of micro-perforated panels using the transfer matrix method. *SAE 2005 noise and vibration conference and exhibition*; 2005.
- [6] Liu J, Herrin DW. Enhancing micro-perforated panel attenuation by partitioning the adjoining cavity. *Appl Acoust* 2010;71:120–7.
- [7] Wang CQ, Huang LX. On the acoustic properties of parallel arrangement of multiple micro-perforated panel absorbers with different cavity depths. *J Acoust Soc Am* 2011;130:208–18.
- [8] Wang CQ, Huang LX, Zhang YM. Oblique incidence sound absorption of parallel arrangement of multiple micro-perforated panel absorbers in a periodic pattern. *J Sound Vib* 2014;333:6828–42.
- [9] Yairi M, Sakagami K, Takebayashi K, Morimoto M. Excess sound absorption at normal incidence by two microperforated panel absorbers with different impedance. *Acoustic Soc Jpn* 2011;32:194–200.
- [10] Tayong R, Dupont T, Leclaire P. Sound absorption of a micro-perforated plate backed by a porous material under high sound excitation: measurement and prediction. *Int J Eng Technol* 2013;2:281–92.
- [11] Dufreche J, Prat M, Schmitz P, Sherwood JD. On the apparent permeability of a porous layer backed by a perforated plate. *Chem Eng Sci* 2002;57:2933–44.
- [12] Sakagami K, Kobatake S, Kano K, Morimoto M, Yairi M. Sound absorption characteristics of a single microperforated panel absorber backed by a porous absorbent layer. *Acoust Aust* 2011;39:95–100.
- [13] Davern WA. Perforated facings backed with porous materials as sound absorbers – experimental-study. *Appl Acoust* 1977;10:85–112.
- [14] Kim S, Kim YH, Jang JH. A theoretical model to predict the low-frequency sound absorption of a Helmholtz resonator array [L]. *J Acoust Soc Am* 2006;119:1933–6.
- [15] Miasa IM, Okuma M, Kishimoto G, Nakahara T. An experimental study of a multi-size microperforated panel absorber. *J Syst Design Dynamics* 2007;1:331–9.
- [16] Park SH. Acoustic properties of micro-perforated panel absorbers backed by Helmholtz resonators for the improvement of low-frequency sound absorption. *J Sound Vib* 2013;332:4895–911.
- [17] Wang CQ, Cheng L, Pan J, Yu GH. Sound absorption of a micro-perforated panel backed by an irregular-shaped cavity. *J Acoust Soc Am* 2010;127:238–46.
- [18] Chen WH, Lee FC, Chiang DM. On the acoustic absorption of porous materials with different surface shapes and perforated plates. *J Sound Vib* 2000;237:337–55.
- [19] Fuchs HV, Zha X, Zhou X, Drotleff H. Creating low-noise environments in communication rooms. *Appl Acoust* 2001;62:1375–96.
- [20] Sanada A, Tanaka N. Extension of the frequency range of resonant sound absorbers using two-degree-of-freedom Helmholtz-based resonators with a flexible panel. *Appl Acoust* 2013;74:509–16.
- [21] Allard JF. Propagation of sound in porous media. London: Elsevier; 1993.
- [22] Atalla N, Sgard F. Modeling of perforated plates and screens using rigid frame porous models. *J Sound Vib* 2007;303:195–208.
- [23] Brennan MJ, To WM. Acoustic properties of rigid-frame porous materials - an engineering perspective. *Appl Acoust* 2001;62:793–811.
- [24] Beranek LL, Vér IL. Noise and vibration control engineering: principles and applications. New York: Wiley; 1992.
- [25] Jung SS, Kim YT, Lee DH, Kim HC, Cho SI, Lee JK. Sound absorption of micro-perforated panel. *J Korean Phys Soc* 2007;50:1044–51.
- [26] Delany ME, Bazley EN. Acoustical properties of fibrous absorbent materials. *Appl Acoust* 1970;3:105–16.
- [27] Yoon GH. Acoustic topology optimization of fibrous material with Delany-Bazley empirical material formulation. *J Sound Vib* 2013;332:1172–87.
- [28] Kim KH, Yoon GH. Optimal rigid and porous material distributions for noise barrier by acoustic topology optimization. *J Sound Vib* 2015;339:123–42.
- [29] Kim YJ, Kim YY. Solid-perforated panel layout optimization by topology optimization based on unified transfer matrix. *J Acoust Soc Am* 2010;128:1777–88.
- [30] Denia FD, Sanchez-Ortiz EM, Martinez-Casas J, Kirby R. Finite element based acoustic analysis of dissipative silencers with high temperature and thermal-induced heterogeneity. *Finite Elem Anal Des* 2015;101:46–57.
- [31] Ingard U. On the theory and design of acoustic resonators. *J Acoust Soc Am* 1953;25:1037–61.
- [32] Bonfiglio P, Pompili F. An acoustic finite element model of perforated elements. In: Proceedings of the COMSOL conference 2009 Milan, Milan; 2009.
- [33] Groby JP, Dazel O, Duclos A, Boeckx L, Kelders L. Enhancing the absorption coefficient of a backed rigid frame porous layer by embedding circular periodic inclusions. *J Acoust Soc Am* 2011;130:3771–80.
- [34] Chevillotte F, Perrot C, Panneton R. Microstructure based model for sound absorption predictions of perforated closed-cell metallic foams. *J Acoust Soc Am* 2010;128:1766–76.
- [35] Pompili F, Bonfiglio P. Acoustical properties of polyurethane open cells materials: Experimental investigation and theoretical models. In: 14th International congress on sound and vibration, Australia; 2007.
- [36] Miki Y. Acoustical properties of porous materials - Modifications of Delany-Bazley models -. *J Acoust Soc Jpn (E)* 1990;11.
- [37] Komatsu T. Improvement of the Delany-Bazley and Miki models for fibrous sound-absorbing materials. *Acoust Sci Tech* 2008;29.
- [38] Vanderplaats GN. Numerical optimization techniques for engineering design: with applications. New York: McGraw-Hill; 1984.